MULTIDIMENSIONAL SLOPE LIMITERS FOR MUSCL-TYPE FINITE VOLUME SCHEMES ON UNSTRUCTURED GRIDS

M.E.Hubbard

The University of Reading,

Department of Mathematics,

P.O.Box 220, Whiteknights,

Reading, RG6 6AX,

United Kingdom

Key words:

MUSCL, upwind schemes, unstructured grids,

slope limiters, conservation laws

Subject classification:

35L65, 65M99, 76M25

Proposed running head:

Improved MUSCL-type schemes on unstructured grids

Address for proofs:

Dr. M.E.Hubbard

The University of Reading

Department of Mathematics

P.O.Box 220

Whiteknights

Reading

RG6 6AX

United Kingdom

Phone: +44 (0)118 9875123 x4009

Fax: +44 (0)118 9313423

Email: M.E.Hubbard@reading.ac.uk

Abstract

A framework is presented for the construction of multidimensional slope limiting operators for two-dimensional MUSCL-type finite volume schemes on triangular grids. A major component of this new viewpoint is the definition of multidimensional 'maximum principle regions'. These are defined by local constraints on the linear reconstruction of the solution which guarantee that an appropriate maximum principle is satisfied. This facilitates both the construction of new schemes and the improvement of existing limiters. It is the latter which constitutes the bulk of this paper. Numerical results are presented for the scalar advection equation and for a nonlinear system, the shallow water equations. The extension to systems is carried out using Roe's approximate Riemann solver. All the techniques presented are readily generalised to three dimensions.

1 Introduction

In one dimension, upwind finite volume schemes have developed into reliable tools for producing accurate numerical approximations of hyperbolic systems of partial differential equations. In higher dimensions it has proved difficult to attain the same degree of robustness and accuracy with simple extensions of these one-dimensional techniques, particularly on unstructured grids. This is in part because the additional multidimensional nature is not exploited sufficiently. As a consequence, a great deal of research has been carried out into the generation of genuinely multidimensional, high order schemes which retain the properties of those methods which have had such success in one dimension.

High resolution schemes for conservation laws in one dimension are usually constructed using some form of TVD (Total Variation Diminishing) limiter (*cf.* [16, 11]) so that high order accuracy can be achieved whilst avoiding unphysical oscillations in the solution. One commonly used approach is the slope limiting (MUSCL) technique of van Leer [17], in which the limiter is applied in a geometric manner, to the gradients of a piecewise linear reconstruction of the solution, to create a monotone scheme. In more than one dimension the generalisation of the TVD condition proves to be prohibitively restrictive on Cartesian meshes because the resulting scheme can be no more than first order accurate [6], and difficult to define on arbitrary unstructured meshes. Consequently, Spekreijse [15] proposed a new class of monotone scheme, based on positivity of coefficients, a property which is simple to define in any number of dimensions. Much subsequent research has been directed towards multidimensional numerical schemes which satisfy properties of this type, usually based on ensuring that some form of local maximum principle is satisfied. More recently, there has

been a great deal of work on limiting reconstructed solutions on unstructured grids, see for example the work of Perthame and Qiu [13] in which interpolated solution values are limited solely to avoid unphysical negative solution values (*e.g.* of density and pressure in the Euler equations), or the Local Extremum Diminishing (LED) schemes of Jameson [10]. More closely related still to the work presented here are the slope limiting procedures for multidimensional cell-centre finite volume schemes for unstructured triangular meshes proposed by Barth and Jespersen [3], Durlofsky *et al.* [4], Liu [12] and Batten *et al.* [2]. Each of these schemes involves the construction of an appropriate linear representation of the solution within a triangular cell which is then limited in a manner which enforces a positivity constraint on the scheme. This paper proposes a way in which these limiting techniques can be improved by taking more account of the multidimensional nature of the problem.

The general two-dimensional MUSCL-type numerical scheme for the solution of the scalar advection equation is described in Section 2. Some existing techniques for reconstructing and limiting the local solution gradients are then discussed briefly, followed by a simple technique for improving the accuracy of many of these limiting procedures. This involves the construction of a 'maximum principle region' for each cell, within which a gradient operator must lie in order to satisfy the desired maximum principle. The framework described also allows the construction of new schemes, but discussion of these is kept to a minimum since a scheme using these ideas has yet to be devised which consistently improves on the existing methods (some preliminary results for a maximally compressive limiter are presented in [8]). This is an area which warrants further research. A critical comparison is then made between the results obtained from the schemes described.

Section 3 extends the applications of these methods to a nonlinear system of equations, specifically the shallow water equations. The basic high order scheme is described, in which Roe's approximate Riemann solver is employed at grid edges, locally decomposing the system into components to which the scalar scheme is applied.

2 The Scalar Advection Equation

In conservation form the two-dimensional scalar advection equation is written

$$u_t + f_x + g_y \;=\; 0 \;, \tag{2.1}$$

where the conservative fluxes $f = f(u)$ and $g = g(u)$ are functions of the solution variable u.

A MUSCL-type cell-centre finite volume method for the numerical solution of the scalar advection equation is described as follows. Integrate (2.1) over a control volume, Ω say, (taken here to be a single grid cell) and apply the divergence theorem to the resulting flux integral, giving the equation

$$\int\!\!\int_{\Omega} u_t \,\mathrm{d}x\,\mathrm{d}y + \oint_{\partial\Omega} \vec{f}\cdot \mathrm{d}\vec{n} \;=\; 0 \;, \tag{2.2}$$

where $\vec{f} = (f,\, g)^{\mathrm{T}}$ is the flux function and $\vec{n}$ represents an outward pointing normal to the boundary $\partial\Omega$ of the control volume.

Approximation of the boundary integral in (2.2) leads to the finite volume discretisation

$$\frac{\mathrm{d}u_0}{\mathrm{d}t} \;=\; -\frac{1}{V_\Omega}\sum_{k=1}^{N_e} \vec{f}^{\,*}_k \cdot \vec{n}_k \;, \tag{2.3}$$

in which u_0 is defined to be the average value of u over the control volume Ω, $\vec{f}^{\,*}_k$ is a numerical flux function, V_Ω is the area of the control volume, N_e is the number

of edges it has and $\vec{n}_k$ is the outward pointing normal to the k^{th} edge, scaled by its length. Note that since the control volumes coincide with the grid cells, the numerical flux function $\vec{f}_k^*$ is an approximation to the flux at a particular grid edge.

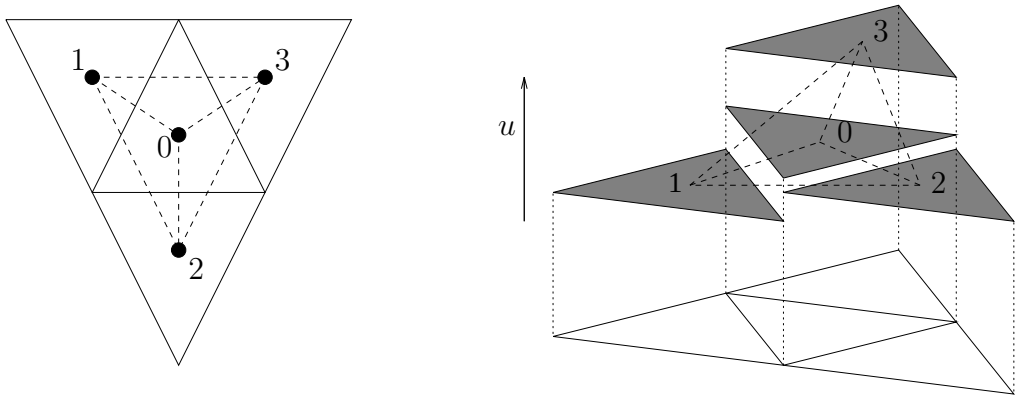

Figure 2.1: The limiting planes as defined for a triangular control volume (left) and a piecewise constant reconstruction of the solution (right).

Assuming that the approximation to u is constant within each cell and discontinuous at the cell edges in general, as illustrated in Figure 2.1, a scheme which is first order accurate in space and satisfies an appropriate local maximum principle is obtained by introducing an upwind bias into the evaluation of the numerical flux function. Taking as an example the k^{th} edge of cell 0 in Figure 2.1, the upwinding is applied [7] by defining

$$\vec{f}^*(u_0, u_k) \cdot \vec{n}_k \;=\; \begin{cases} u_0 \, \tilde{\vec{\lambda}} \cdot \vec{n}_k & \text{if } \; \tilde{\vec{\lambda}} \cdot \vec{n}_k \geq 0 \\ u_k \, \tilde{\vec{\lambda}} \cdot \vec{n}_k & \text{otherwise} \, , \end{cases} \tag{2.4}$$

where u_k is the value of u in the adjacent grid cell and $\tilde{\vec{\lambda}}$ is an appropriate local average of the advection velocity $\vec{\lambda} = \left(\frac{\partial f}{\partial u}, \frac{\partial g}{\partial u}\right)^{\mathrm{T}}$, evaluated from the solution values u_0 and u_k. Note that an equivalent expression to (2.4) is given by

$$\vec{f}^*(u_0, u_k) \cdot \vec{n}_k \;=\; \frac{1}{2}(\vec{f}_0 + \vec{f}_k) \cdot \vec{n}_k - \frac{1}{2} |\tilde{\vec{\lambda}} \cdot \vec{n}_k| (u_k - u_0) \, , \tag{2.5}$$

which is generally preferred because of its symmetry. Although only triangular grid cells are illustrated in Figure 2.1, the numerical fluxes (2.4) and (2.5) can be used on general polygonal cells, such as quadrilaterals.

2.1 Gradient Operators and Higher Order Schemes

Higher order spatial accuracy is achieved by introducing a higher order reconstruction of the variable u within each grid cell. For example, a piecewise linear approximation to the solution, such as that shown in Figure 2.2, which is exact for linear initial data, leads to a method which is second order accurate in space.

Thus, given an initial constant (or average) solution value $\overline{u}$ within a cell we carry out a linear reconstruction of u within that cell. This is expressed as

$$u \;=\; \overline{u} + \vec{r} \cdot \vec{L}\,, \tag{2.6}$$

where $\vec{r}$ is a position vector relative to the centroid of the cell and $\vec{L}$ is a gradient operator, yet to be defined. It is easy to show that such a reconstruction is conservative in the sense that

$$\frac{1}{V_\Omega} \int\!\!\int_\Omega u \, \mathrm{d}x \, \mathrm{d}y \;=\; \overline{u}\,. \tag{2.7}$$

It can also be shown [2] that when (2.7) holds the resulting numerical scheme (2.3) will satisfy a local maximum principle for an appropriate restriction on the time-step as long as the reconstruction (2.6) within each cell does not lead to the creation of any new extrema at the *midpoints* of the edges of that cell. This is less restrictive than the often used constraint [3] that no new extrema be created at the cell vertices.

The numerical flux function of Equation (2.5) at a cell edge is now written in terms of the reconstructed solution values in the cells on either side of the edge and

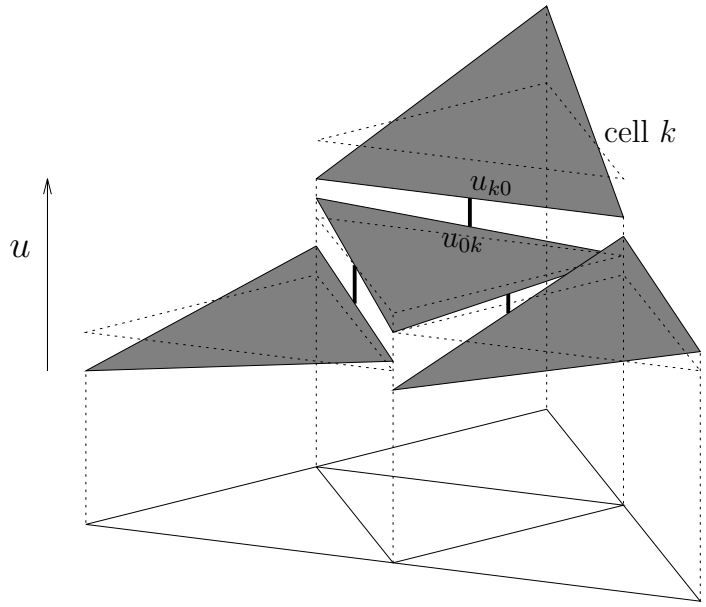

Figure 2.2: A piecewise linear reconstruction of the solution for triangular control volumes.

evaluated at the midpoint, as depicted in Figure 2.2. Thus, $\vec{f}^*$, as substituted into (2.3) is written

$$\vec{f}_k^* \;=\; \vec{f}^*(u_{0k}, u_{k0}) \;=\; \vec{f}^*(u_0 + \vec{r}_{0k} \cdot \vec{L}_0,\; u_k + \vec{r}_{k0} \cdot \vec{L}_k) \;, \tag{2.8}$$

where $\vec{r}_{ij}$ is the vector from the centroid of cell i to the midpoint of the edge between cells i and j, and $\vec{L}_i$ is the gradient of the reconstructed solution in cell i. In the notation used here u_{0k} is considered to be an *interior* reconstructed solution value relative to the cell under consideration and u_{k0} is the corresponding *exterior* value, taken from the adjacent cell (see Figure 2.2). As in the MUSCL approach, the discontinuity in the reconstruction at the cell edge motivates the use of a Riemann solver to evaluate the fluxes here. It remains to define an appropriate gradient operator $\vec{L}$ with which to create the linear reconstruction of the solution within each grid cell.

A simple gradient operator, which is exact for linear data, can be defined on any grid by taking the (average) solution value in three arbitrarily chosen, but preferably

adjacent, cells (i, j and k say, forming a triangle with anticlockwise indexing of its vertices) and defining

$$\vec{\nabla}(\triangle ijk) \;=\; \begin{cases} \begin{pmatrix} -\frac{n_x}{n_u} \\ -\frac{n_y}{n_u} \end{pmatrix} & \text{for} \quad n_u \geq \epsilon \\ \begin{pmatrix} 0 \\ 0 \end{pmatrix} & \text{otherwise .} \end{cases} \tag{2.9}$$

Here $\epsilon \approx 10^{-10}$ is a specified tolerance, and n_x, n_y and n_u are the components of the vector $\mathbf{n}$ normal to the plane, defined by the triangle ijk in xyu-space, *cf.* Figure 2.1, and given by

$$\mathbf{n} \;=\; (\underline{P}_i - \underline{P}_k) \times (\underline{P}_j - \underline{P}_k) \;, \tag{2.10}$$

where

$$\underline{P}_* \;=\; \begin{pmatrix} x_* \\ y_* \\ u_* \end{pmatrix} \;. \tag{2.11}$$

The vector $\vec{n}$ has been constructed in such a way that n_u always has the same sign as the area of $\triangle ijk$. The second option in (2.9) deals with the possibility of $\triangle ijk$ having a non-positive area and rejects any such triangle as a basis for reconstruction. Figure 2.3 illustrates that this can happen even on relatively uniform grids. Note also that any consistent local approximation to $\vec{\nabla}u$ may be used in place of (2.9), *e.g.* the Green-Gauss and Linear Least-Squares approximations used in [3].

Selecting $\vec{L}$ in (2.8) to be the $\vec{\nabla}$ operator of (2.9) leads to a second order accurate method (a linear solution is modelled exactly) but doesn't prohibit overshoots and undershoots at the midpoints of the cell edges, so the scheme does not satisfy a local maximum principle. In order to impose this the gradient operator $\vec{L}$ must be defined as a 'limited' form of $\vec{\nabla}$.

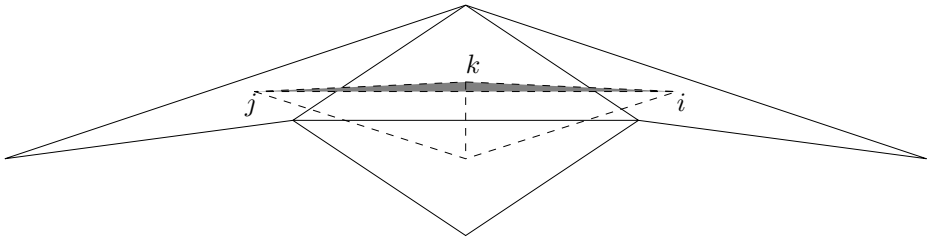

Figure 2.3: A reconstruction triangle with negative area (shaded).

2.1.1 Limited Gradient Operators

The imposition of a local maximum principle, as used in the work of [12, 4, 2], can be achieved by constraining the gradient operator to lie within a 'Maximum Principle (MP) region'. The MP region for a given triangle can be represented simply by choosing the cell centroid as the origin and then constructing the region around it defined by the inequalities

$$\min\left(u_k - u_0, 0\right) \;\leq\; \vec{r}_{0k} \cdot \vec{L} \;\leq\; \max\left(u_k - u_0, 0\right) \tag{2.12}$$

for $k = 1, 2, 3$ (on triangles), where $\vec{r}_{0k}$ is the vector from the centroid of cell 0 to the midpoint of the edge between cells 0 and k. An example of such a region is depicted in Figure 2.4. The gradient operator $\vec{L} = (x, y)^{\mathrm{T}}$ is most easily considered as a vector in two-dimensional space; then each pair of inequalities in (2.12) can be depicted by two parallel lines (one solid and one dashed in the figure) perpendicular to the relevant vector $\vec{r}_{0k}$. Figure 2.4 illustrates a case where $u_1, u_2 > u_0$ and $u_3 < u_0$. If $u_k - u_0$ has the same sign for each k then the MP region contains only the centroid of the triangle, as would be expected since this indicates a local extremum. Hence, any limiting procedure of the type considered in (2.12) reduces the scheme locally to first order in these cases.

However, the constraints given by (2.12) ensure that the reconstruction has the

following two properties:

- no new solution extrema are created at the midpoints of the cell edges, enforcing the maximum principle.

- $u_{0k} - u_0$ has the same sign as $u_k - u_0$.

Note that this differs from the work of Barth and Jesperson [3] who, in addition, propose that

- $u_{k0} - u_{0k}$ has the same sign as $u_k - u_0$.

This, in combination with the other two properties, generalises the one-dimensional TVD constraint on the reconstruction, but it is not necessary for positivity and, as in [4, 12, 2], is not enforced in this work. It is not clear how a MP region could be constructed which would ensure the third property, but a simple post-processing step, in which the reconstructed solution within the offending cells is limited a second time (so that $\vec{L} \to \alpha^* \vec{L}$), would be enough to attain it.

Existing limited schemes based on (2.9) can be expressed quite simply, in two stages, as

a) Construct one or more of the gradient operators

$$\vec{\nabla}(\triangle 123)\ ,\quad \vec{\nabla}(\triangle 023)\ ,\quad \vec{\nabla}(\triangle 103)\ ,\quad \vec{\nabla}(\triangle 120)\ , \tag{2.13}$$

(in the notation of (2.9) and Figure 2.1).

b) Limit a gradient operator chosen from (2.13).

Importantly, the first of these two steps ensures that the reconstruction of a linear solution is exact (for higher order accuracy), whichever of the four gradient operators

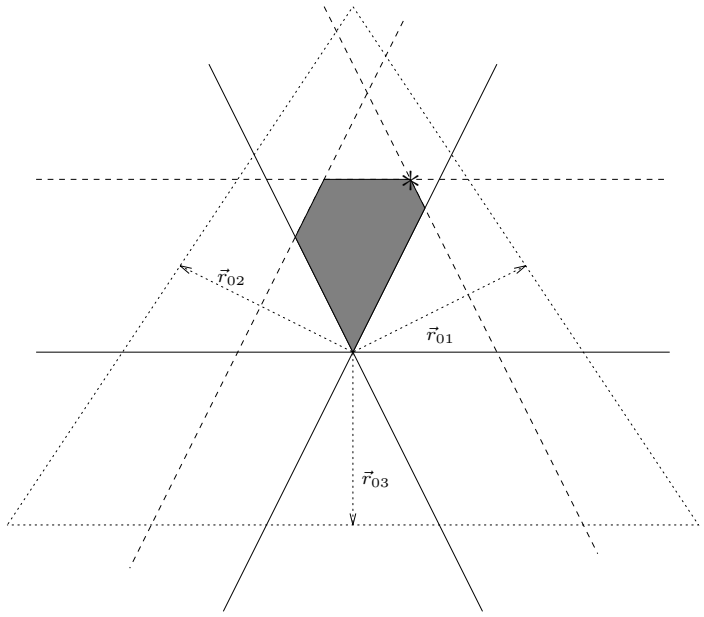

Figure 2.4: A Maximum Principle region (shaded).

is chosen, and the limiting procedure will not interfere with this. As mentioned earlier, the list given in (2.13) can be augmented by the Green-Gauss ($\vec{\nabla}_{\mathrm{GG}}$) and the Linear Least-Squares ($\vec{\nabla}_{\mathrm{LLS}}$) gradient reconstructions suggested in [3], both of which can be treated in the same manner in the second stage. In effect, step a) defines a finite set of possible directions for the reconstructed gradient, and step b) chooses one of these directions and bounds the magnitude of the slope.

The Limited Central Difference (LCD) scheme is the simplest and cheapest approach of the type described above. It considers only the operator $\vec{\nabla}(\triangle 123)$ in step a), and then limits this by setting

$$\alpha^k \;=\; \begin{cases} \frac{\max\left(u_k-u_0,0\right)}{\vec{r}_{0k}\cdot\vec{L}} & \text{if } \; \vec{r}_{0k}\cdot\vec{L} \;>\; \max\left(u_k-u_0,0\right) \\ \frac{\min\left(u_k-u_0,0\right)}{\vec{r}_{0k}\cdot\vec{L}} & \text{if } \; \vec{r}_{0k}\cdot\vec{L} \;<\; \min\left(u_k-u_0,0\right) \\ 1 & \text{otherwise} \end{cases} \tag{2.14}$$

for each edge k, from which the LCD gradient operator is calculated using

$$\vec{L}_{\mathrm{LCD}} \;=\; \alpha\,\vec{\nabla}(\triangle 123) \;=\; \left(\min_{k=1,2,3}\alpha^k\right)\vec{\nabla}(\triangle 123)\,. \tag{2.15}$$

The action of this limiter is illustrated in Figure 2.5. The initial operator $\vec{\nabla}(\triangle 123)$ might place the tip of the vector $\vec{L} = (x, y)^{\mathrm{T}}$ at any one of the four points indicated by asterisks in the figure. Point A is inside the shaded region and so is unaffected by the limiting, while points B, C and D all lie beyond the region, and the limiting moves them in a straight line back towards the centroid until they reach the boundary of the MP region: for points C and D this means a return to the centroid and a first order reconstruction.

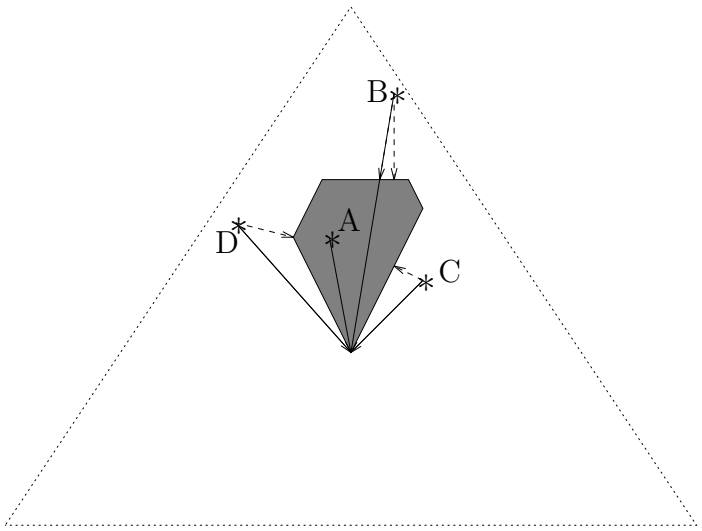

Figure 2.5: The alternative limiting procedures.

Figure 2.5 also depicts an alternative limiting procedure, aimed at improving the accuracy. Instead of retaining the direction of the original gradient operator, the limited gradient is defined by the point in the MP region closest to the tip of the vector $\vec{L}$. The dashed arrows indicate the consequent movement of the points B, C and D. Points such as C and D are most simply dealt with by a projection step (on to the lines passing through the centroid perpendicular to $\vec{r}_{02}$ and $\vec{r}_{01}$ respectively) to obtain the gradient direction, followed by a limiting step which moves the point

on to the boundary of the region if it still remains outside. In practice, however, the expense of changing the limiting procedure for point B outweighs the resulting improvement in accuracy so the simpler strategy is applied in such cases.

The limiter of Durlofsky *et al.* [4] considers the last three gradient operators of (2.13) together with $\vec{L} = \vec{0}$, discards those which lie outside the MP region and then chooses $\vec{L}_{\text{Durl}}$ to be the remaining operator with greatest magnitude.

The Maximum Limited Gradient (MLG) scheme of Batten *et al.* [2] combines the two methodologies described above. It takes all four of the operators of (2.13), limits each one in turn in the manner of the LCD scheme (2.14, 2.15) and then takes $\vec{L}_{\text{MLG}}$ to be the remaining operator with largest slope $|\vec{L}|$. Figure 2.5 can again be used as an illustration. If the asterisks represent the four gradient operators in (2.13) then each one is limited individually in precisely the manner of the LCD scheme, moving the gradients into the allowed range, and the point furthest away from the cell centroid is chosen - in this case the limited position of point B. As with the LCD scheme the alternative technique of projecting the gradient operators on to the boundary of the MP region can be used to improve the accuracy, although the resulting scheme can be prohibitively expensive.

The MLG scheme gives the most compressive of the limiters described so far, and the only one which reduces to the Superbee limiter [16] in one dimension, but it is also the most expensive since it requires the computation of four gradient planes. An even more accurate scheme (but yet more expensive) can be devised by including the Green-Gauss and Limited Least-Squares operators [3] in (2.13) and applying the MLG procedure to these as well. For practical purposes though, it is desirable to construct as few gradient operators as possible.

It should be noted that the neither the MLG, the Durlofsky nor the LCD scheme depends continuously on the solution data, since the limited gradient operator changes discontinuously as the operator on which it is based moves out of the sector enclosing the MP region (see Figure 2.5). Whilst this is of little consequence for genuinely time-dependent problems, it may interfere with convergence to a steady state by causing limit cycling. The inclusion of the 'projection' step in the limiting procedure makes the LCD scheme continuous as well as improving its accuracy. It is also worth commenting that the general limiting procedure, as described by steps a) and b) earlier in this section, can easily be extended to arbitrary polygonal/polyhedral control volumes in two and three dimensions [8]. However, on structured quadrilateral grids this method is considerably more diffusive than using a standard, dimensionally split scheme, see for example [1], which is linearity preserving on the uniform grids used here (although it might not be on distorted grids).

A final point to make in this section is that the construction of the MP region facilitates the creation of a range of new limited gradient operators satisfying the given maximum principle, even though they can generally only be imposed in a rather artificial manner. For example, the steepest gradient operator which satisfies the maximum principle is defined by the point in the MP region farthest away from the centroid of the triangle (which is always a 'corner' of the region, as indicated by an asterisk for the case shown in Figure 2.4), and this can be taken to be the limited gradient, but only when a necessity for limiting is indicated. Further details and preliminary results can be found in [8] and provides a subject for further research.

A scheme of this form, as applied on a triangular grid, can be summarised as

follows:

- Calculate the gradient operator $\vec{\nabla}(\triangle 123)$ as in the LCD scheme and check whether it creates any new local extrema at the edge midpoints.
  - if not, select $\vec{L} = \vec{\nabla}(\triangle 123)$.
  - otherwise calculate the new gradient operator $\vec{L}$, *e.g.* the one with maximal slope which still satisfies the local maximum principle.

Finding a gradient operator of this type is relatively expensive, so it should only be calculated in cells where the initial reconstruction gives rise to overshoots or undershoots. This process is significantly cheaper than finding the three other gradient operators of the MLG limiter. In fact the local maximum principle could be checked for all four gradient operators of the MLG limiter (2.13), but the extra compression which results does not justify the computational expense.

2.2 Boundaries

The limiting procedure is applied very simply at boundaries of the domain. In step a) of the limiting procedure only those gradient operators which can be constructed from centroids of control volumes *within* the domain are included and the others are assumed to be zero. Also, only internal solution values are considered in the search for new extrema in the reconstruction. On a triangular grid this means that only a single gradient operator is constructed (and limited) in each cell with just one boundary edge. (For the LCD scheme this replaces the usual gradient operator.) The scheme therefore produces an exact reconstruction of linear data on triangles except in cells with multiple boundary edges. The fluxes through the inflow boundary edges are

overwritten by their exact values. When periodic boundary conditions are used no special treatment of the boundaries is needed.

2.3 Time Integration

Second order temporal accuracy may be obtained using a Runge-Kutta time-stepping method such as

$$\begin{aligned} \overline{u}_0 &= u_0^n - \frac{\Delta t}{V}\sum_{k=1}^{N_e} \vec{f}\left(u_0^n + \vec{r}_{0k}\cdot\vec{L}_0^n,\, u_k^n + \vec{r}_{k0}\cdot\vec{L}_k^n\right)\cdot\vec{n}_k \\ u_0^{n+1} &= \frac{1}{2}\left(u_0^n + \overline{u}_0 - \frac{\Delta t}{V}\sum_{k=1}^{N_e} \vec{f}\left(\overline{u}_0 + \vec{r}_{0k}\cdot\overline{\vec{L}}_0,\, \overline{u}_k + \vec{r}_{k0}\cdot\overline{\vec{L}}_k\right)\cdot\vec{n}_k\right) \\ &= u_0^n - \frac{\Delta t}{2V}(\delta u_0 + \delta\overline{u}_0)\ . \end{aligned} \tag{2.16}$$

However, the cost of the reconstructions and the local Riemann solutions is prohibitively expensive, so the following approximation to the above explicit update scheme [18] is used instead:

$$\begin{aligned} \overline{u}_0 &= u_0^n - \frac{\Delta t}{2V}\sum_{k=1}^{N_e} \vec{f}\left(u_0^n + \vec{r}_{0k}\cdot\vec{L}_0^n\right)\cdot\vec{n}_k \\ u_0^{n+1} &= u_0^n - \frac{\Delta t}{V}\sum_{k=1}^{N_e} \vec{f}\left(\overline{u}_0 + \vec{r}_{0k}\cdot\vec{L}_0^n,\, \overline{u}_k + \vec{r}_{k0}\cdot\vec{L}_k^n\right)\cdot\vec{n}_k\ . \end{aligned} \tag{2.17}$$

It has been shown [2] that on triangular grids any limiter of the type described in this paper satisfies the maximum principle for a restriction on the time-step within each cell given by

$$\Delta t \ \leq\ \frac{V}{3\max_k|\tilde{\vec{\lambda}}\cdot\vec{n}_k|}\ . \tag{2.18}$$

The maximum is taken over the adjacent cells indexed here by k. Note that a slight drawback with the simplified scheme (2.17) is that it may allow small overshoots and undershoots to appear in the solution. However, these do not interfere noticeably with the overall robustness of the algorithm.

2.4 Results

Numerical experiments have been carried out to test the behaviour of the schemes described in this paper. The first test presented here is the advection of an initial profile given by the double sine wave function

$$u \;=\; \sin(2\pi x)\sin(2\pi y)\;, \tag{2.19}$$

with velocity $\vec{\lambda} = (1, 2)^{\mathrm{T}}$ over the domain $[0, 1] \times [0, 1]$. This problem has been solved on three types of grid, each of which is illustrated in Figure 2.6. Periodic boundary conditions are applied. Note that the advection velocity has been chosen so that it is not aligned with mesh edges, to provide a more strenuous test than was used to produce the accuracy study of schemes of this type presented in [2], and hence there is some loss of accuracy in comparison.

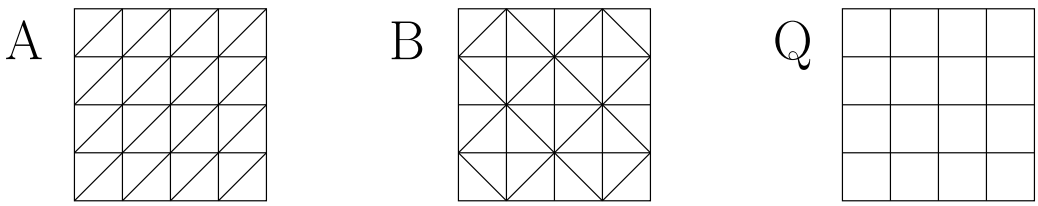

Figure 2.6: The three grid types used for the numerical experiments.

Errors in the L_1 and L_∞ norms for the solutions obtained when $t = 1.0$ are shown in Figures 2.7 and 2.8. In all of the numerical experiments the ratio $\Delta t/\Delta x = 0.16$, where Δx is the length of any horizontal grid edge in Figure 2.6, giving a CFL of about 0.358.

The first order scheme is unsurprisingly the least accurate in each case, while the unlimited scheme is easily the best: it is the oscillations it allows in solutions with rapidly varying gradients which cause problems when applied to nonlinear systems

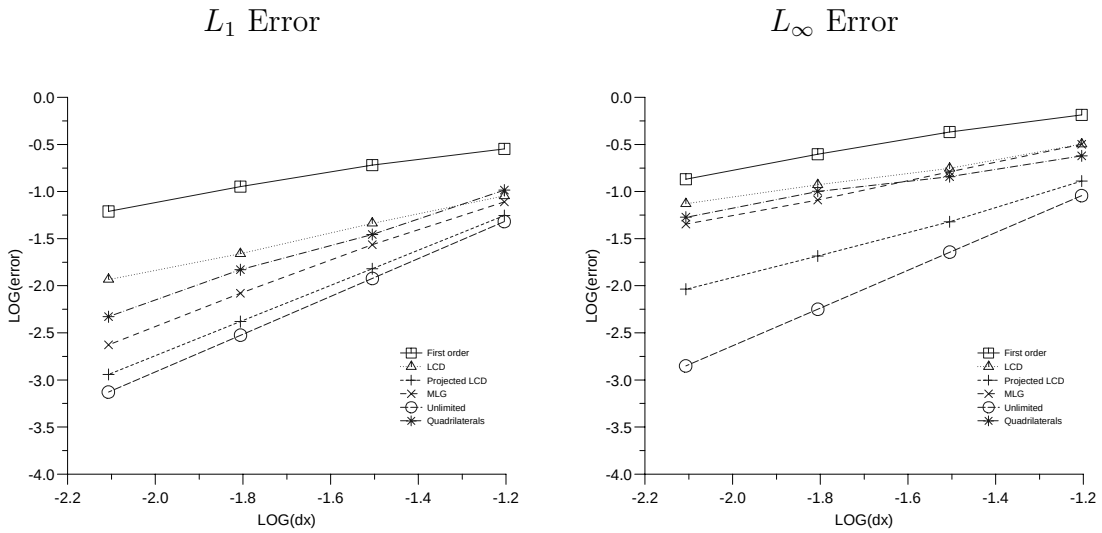

Figure 2.7: Errors for the double sine wave test case on grid A.

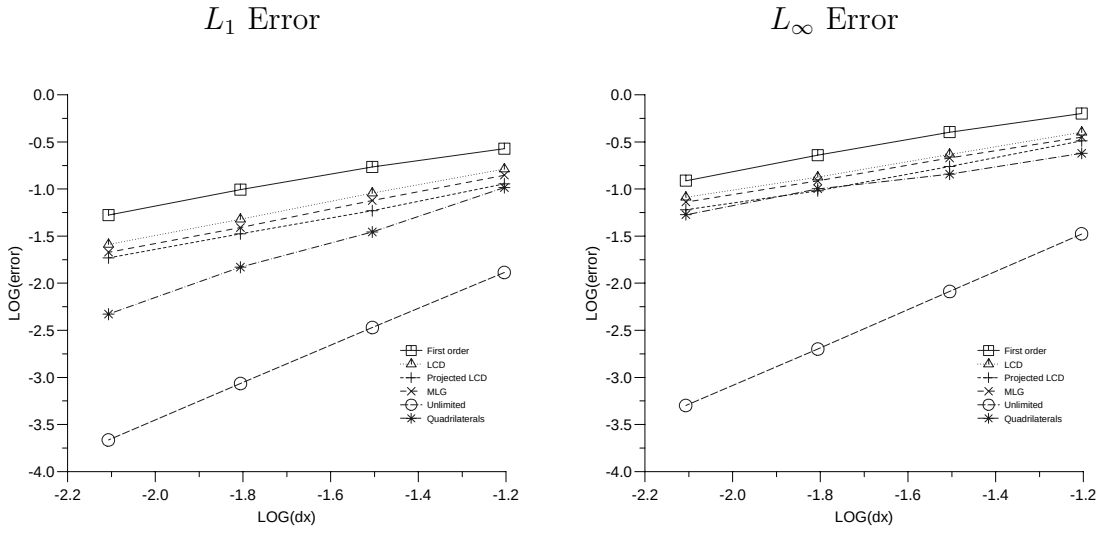

Figure 2.8: Errors for the double sine wave test case on grid B.

since they can lead to unphysical situations. On grid B each of the higher order schemes produces very similar results, none of which can compete with the accuracy attained on a uniform quadrilateral grid of type Q (using a dimensionally split upwind scheme with the Superbee limiter [16]), particularly when taking into account the fact that this grid contains only half the number of cells of the others. It can be seen from Table I that none of the limited schemes achieves even first order accuracy on the finest grids tested. This seems to be due to the anisotropic connectivity of this type of grid and its effect on the limiting procedure. In essence, the limiting is applied to solution values at the midpoints of the cell edges. On type A grids these lie on the midpoints of the straight lines joining the cell centroids (see Figure 2.9), so the limiting procedure gives higher accuracy than on grid B where this is not generally the case. Furthermore, grid B will generally give a smaller MP region, simply because the bounds in (2.12) are tighter due to the centroids of the adjacent triangles being closer together which will generally give a smaller difference in u between cell centres.

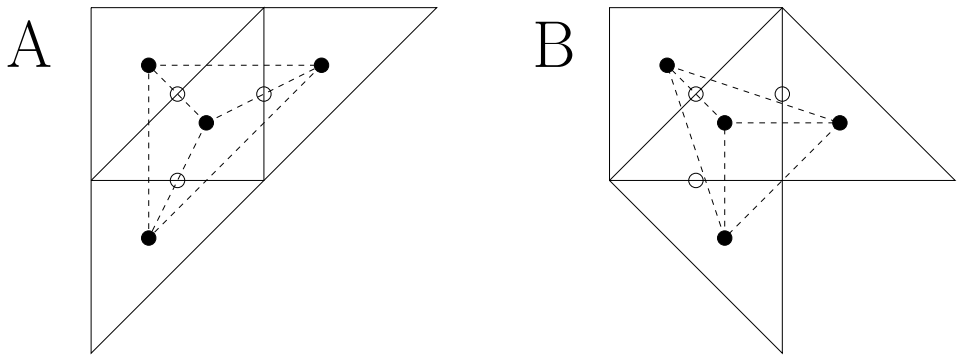

Figure 2.9: Bounding points (circles) for the limiting of the reconstruction for the two grid types.

Note that other schemes which calculate only a single gradient operator, such as Limited Least-Squares [3], produce results which are almost indistinguishable from

those of the LCD scheme and so they are not presented here.

On type A grids the advantages of adding the projection step to the limiting procedure become clear, particularly in the comparisons of the L_∞ error. The projected LCD scheme provides a clear improvement, even over the solution obtained on the quadrilateral grid. When taking into account the differing numbers of grid cells (which would shift the graph of the quadrilateral scheme 0.15 to the right), the projected LCD scheme still produces a solution of a prescribed accuracy faster than the structured grid schemes. (The figures given as times in Table I are relative to the time taken to calculate the first order solution and are all found for 64×64 grids.) On the finest grids though, it is the MLG scheme which achieves the highest order of accuracy in terms of the L_1 error, the wider choice of gradient operators being more useful here than the projection of a single one.

	Grid type A				Grid type B		
Scheme	Time	L_1	L_∞	Peak	L_1	L_∞	Peak
First order	1.00	0.87	0.88	0.23	0.90	0.90	0.28
LCD	1.32	0.91	0.67	0.52	0.88	0.70	0.48
Projected LCD	1.50	1.87	1.17	0.85	0.85	0.67	0.68
MLG	1.73	1.82	0.85	0.93	0.87	0.75	0.62
Unlimited	1.23	2.00	2.00	0.95	1.99	1.99	0.96
Quadrilaterals	0.75	1.65	0.91	0.86	1.65	0.91	0.86

Table I: Numerical orders of accuracy and relative cpu times for the double sine wave test case and peak solution values for the rotating cone test case.

A second test case has been used to further clarify the relative merits of the given

schemes. It involves the circular advection of the 'cone', given by the initial conditions (when $t = 0.0$)

$$u = \begin{cases} \cos^2(2\pi r) & \text{for } r \leq 0.25 \\ 0 & \text{otherwise} \end{cases} \tag{2.20}$$

where $r^2 = (x + 0.5)^2 + y^2$, with velocity $\vec{\lambda} = (-2\pi y, 2\pi x)^{\mathrm{T}}$ around the domain $[-1, 1] \times [-1, 1]$, with zero conditions at each of the inflow boundaries. The initial profile should be advected in a circle without change of shape until it returns to its original position when $t = 1.0$.

Solution profiles obtained on 64×64 grids of types A and B are shown in Figures 2.10 and 2.11 respectively. The maximum CFL within the computational domain was 0.355. The corresponding peak solution values are shown in Table I. Of the schemes presented on triangular grids, MLG is clearly the most compressive on grid type A, confirming what was seen for the first test case, although there is some small upstream distortion of the profile. This is not apparent in the projected LCD solution and this is considerably better than the standard LCD approach. However, none of the unstructured grid schemes matches the performance of the dimensionally split Superbee limited upwinding on quadrilaterals. On grid B the projected LCD scheme is now the best of the triangular grid methods. There is little to choose between the solutions obtained from this and the MLG scheme, but the relative cpu times in Table I indicate the greater efficiency of the former.

In general, it can be seen that the multidimensional projection step improves the LCD scheme considerably, to the point where the solutions are at least as accurate as those produced by the more expensive MLG scheme on all but the most uniform grids. Using the projection step also seems to be particularly advantageous for reducing the

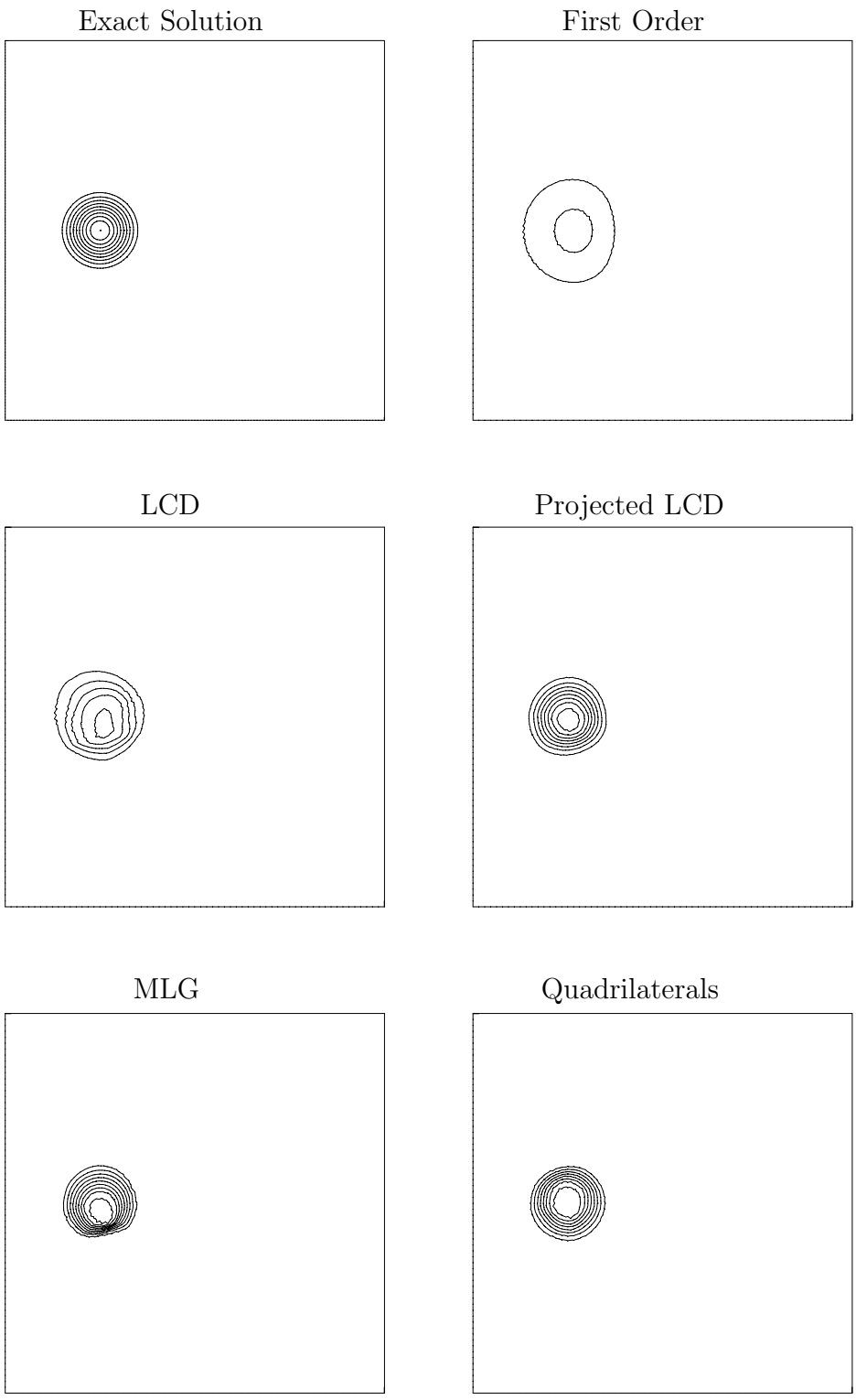

Figure 2.10: Solutions for the rotating cone test case on grid type A.

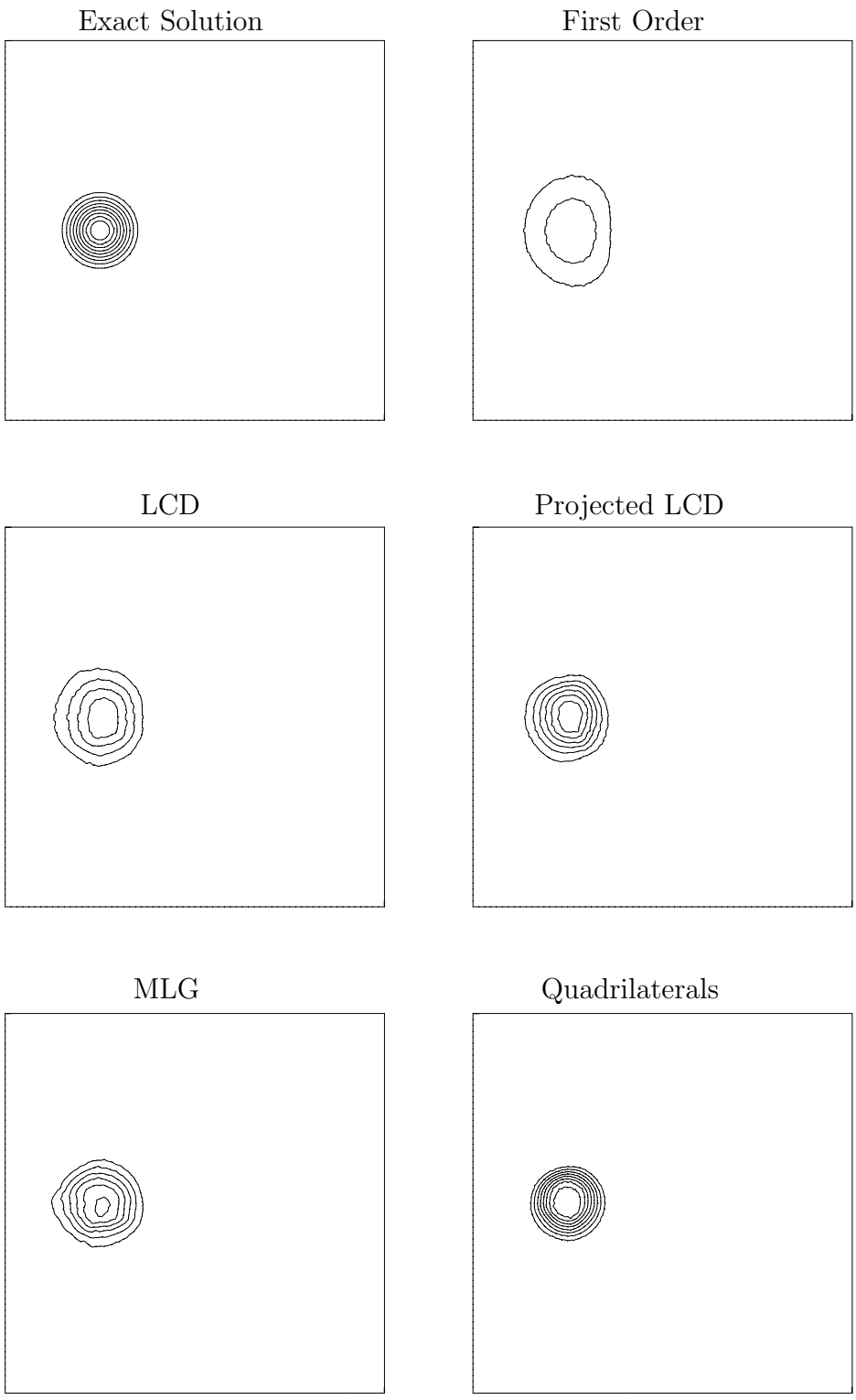

Figure 2.11: Solutions for the rotating cone test case on grid type B.

errors in the L_∞ norm.

3 Systems of Equations

The extension of these cell centred MUSCL-type finite volume schemes to nonlinear systems of equations is straightforward. The conservative equations take the general form

$$\underline{U}_t + \underline{F}_x + \underline{G}_y \;=\; \underline{0}\,, \tag{3.1}$$

in which $\underline{U}$ is the vector of conserved variables and $\underline{F}$, $\underline{G}$ are the conservative flux vectors. These are defined explicitly for the shallow water equations in Appendix A.

Integrating the equations (3.1) over a control volume Ω (taken as before to be a grid cell) and applying the divergence theorem to the flux integral results in

$$\int\!\!\int_\Omega \underline{U}_t \,\mathrm{d}x\,\mathrm{d}y + \oint_{\partial\Omega} (\underline{F},\, \underline{G}) \cdot \mathrm{d}\vec{n} \;=\; 0\,, \tag{3.2}$$

where $\vec{n}$ again represents an outward pointing normal to the boundary. Approximating the boundary integral and defining $\underline{U}_0$ to be the average value of $\underline{U}$ over the control volume Ω leads to the finite volume discretisation

$$\frac{\partial \underline{U}_0}{\partial t} \;=\; -\frac{1}{V_\Omega} \sum_{k=1}^{N_e} (\underline{F}^*_k,\, \underline{G}^*_k) \cdot \vec{n}_k\,, \tag{3.3}$$

where $\underline{F}^*_k$ and $\underline{G}^*_k$ are the numerical flux functions, V_Ω is the area of the control volume, N_e is the number of edges of the control volume and $\vec{n}_k$ is the outward pointing normal to the k^{th} edge, scaled by its length.

The generalisation of the first order scalar numerical flux function of (2.5) to systems of equations is given by

$$\begin{aligned}(\underline{F}^*(\underline{U}_0, \underline{U}_k), \underline{G}^*(\underline{U}_0, \underline{U}_k)) \cdot \vec{n}_k \;=\;& \tfrac{1}{2}\left((\underline{F}_0, \underline{G}_0) + (\underline{F}_k, \underline{G}_k)\right) \cdot \vec{n}_k \\ & -\tfrac{1}{2}|(\tilde{\mathbf{A}}, \tilde{\mathbf{B}}) \cdot \vec{n}_k|(\underline{U}_k - \underline{U}_0)\,,\end{aligned} \tag{3.4}$$

in which $\mathbf{A} = \frac{\partial \underline{F}}{\partial \underline{U}}$ and $\mathbf{B} = \frac{\partial \underline{G}}{\partial \underline{U}}$ are the flux Jacobians. The construction of $\tilde{\mathbf{A}}$ and $\tilde{\mathbf{B}}$, the conservative approximations to the Jacobian matrices, and subsequently the numerical flux at the midpoint of the cell edge follows the technique suggested by Roe [14].

The evolution of the discontinuous approximation to the solution is modelled by constructing a series of approximate Riemann problems at the edge midpoints with 'left' and 'right' states, $\underline{U}_{0k}$ and $\underline{U}_{k0}$ respectively at edge k (the internal and external states relative to the control volume), of the *reconstructed* solution, *cf.* Equation (2.8) and Figure 2.2. Each Riemann problem is solved using the decomposition of the flux difference across the edge into its characteristic components. This results in a high order numerical flux function for edge k given by

$$\begin{aligned}(\underline{F}^*(\underline{U}_{0k}, \underline{U}_{k0}), \underline{G}^*(\underline{U}_{0k}, \underline{U}_{k0})) \cdot \vec{n}_k \;=\; & \tfrac{1}{2}\left((\underline{F}_{0k}, \underline{G}_{0k}) + (\underline{F}_{k0}, \underline{G}_{k0})\right) \cdot \vec{n}_k \\ & - \tfrac{1}{2} \textstyle\sum_{j=1}^{N_w} \tilde{\alpha}^j |\tilde{\lambda}^j| \tilde{\underline{r}}^j \; . \end{aligned} \tag{3.5}$$

Here N_w is the number of components (or 'waves') in the decomposition, the tilde represents the Roe average value at the discontinuity (which is constructed so as to ensure that the linearised decomposition is conservative [14]); α^j is a wave 'strength'; λ^j and $\underline{r}^j$, respectively the eigenvalues and eigenvectors of the matrix $(\mathbf{A}, \mathbf{B}) \cdot \vec{n}_k$, represent the speed of the wave and the transformation of a perturbation of the characteristic variables into a perturbation of the conservative variables. Details of the exact values of these averages for the shallow water equations are supplied in Appendix A. The substitution of (3.5) into (3.3) together with the application of an appropriate time-stepping scheme (see Section 2.3) gives the final algorithm.

The slope limiting is commonly applied to the primitive variables which, for the Euler equations ensures a positive reconstruction of both density *and* pressure (al-

though this may not be maintained by the subsequent application of Roe's approximate Riemann solver). For the shallow water equations both primitive and conservative variable limiting give positive depths so there is less advantage in using the former, which is also slightly more expensive. Here the limiters are applied directly to the conservative variables, mainly for the purposes of speed and simplicity. In many ways characteristic limiting would seem to be the most natural implementation, see for example [2], but its application to Roe's scheme is not straightforward [8], and the results are not improved greatly so they are not presented here.

3.1 Boundary Conditions

Simple characteristic boundary conditions are applied, in which the flux at a boundary edge is evaluated directly using information from within the boundary cell to supplement the imposed boundary values. The physical conditions applied at a given edge correspond to the positive eigenvalues of the matrix $\mathbf{C} = \mathbf{A}\cos\theta + \mathbf{B}\sin\theta$, where $(\cos\theta, \sin\theta)^{\mathrm{T}}$ is the local unit inward normal to the boundary. The conservative flux Jacobian matrices $\mathbf{A}$ and $\mathbf{B}$ are given for the shallow water equations in Appendix A.

At a freestream boundary four possibilities arise: (a) supercritical inflow, where all three eigenvalues are positive and the boundary flux is determined completely by the imposed solution values; (b) supercritical outflow, where no eigenvalue is positive and the flux is calculated from internal solution values; (c) subcritical inflow, where one eigenvalue is negative and whose corresponding Riemann invariant is given its internal value with everything else imposed; and finally (d) subcritical outflow, for which one eigenvalue is positive and only the value of its associated Riemann invariant is imposed. At a solid wall the normal velocity component is set to zero while the

rest of the information required to calculate the flux is taken from the interior of the domain.

3.2 Results

The first test case considered here is a simple steady state problem with an exact solution, represented by an oblique hydraulic jump in a channel induced by a wedge [1]. The geometry of the channel is indicated in Figure 3.1: it is 40m long, 30m wide at inflow and the foot of the wedge is 10m in from the inflow boundary. The slope of the wedge is chosen here to be 8.95°, and inflow conditions of $h = 1.0$m, $u = 8.57\text{ms}^{-1}$ and $v = 0.0\text{ms}^{-1}$ (implying a Froude number of $F = 2.74$) are imposed. The resulting steady state flow should be purely supercritical and divided into two regions by an oblique hydraulic jump at an angle of 30° to the upstream flow. Downstream of this jump the exact solution is given by $h_d = 1.5$m and $F_d = 2.074$.

Three solutions are illustrated in Figure 3.1 and there is little to choose between them. The final solution was obtained using a dimensionally split, van Leer limited scheme on a regular 40×30 cell quadrilateral grid, giving the same mesh scale as the 2609 cell triangular grid shown, but fewer cells, so it is unsurprising that this appears to be the most diffusive of the schemes. When sampling the solution at a point on the outflow boundary midway between the lower wall and the jump, each of the schemes predicted the downstream flow parameters accurate to two decimal places.

The next test case presented is of shallow water flow for a partial dam break problem [5]. The computational domain consists of a 200m $\times$ 200m basin bisected by a dam. When $t = 0.0$s a break in the dam appears between 95m and 170m from one end. Initially $h = 10$m on one side and $h = 5$m on the other, while the water has zero

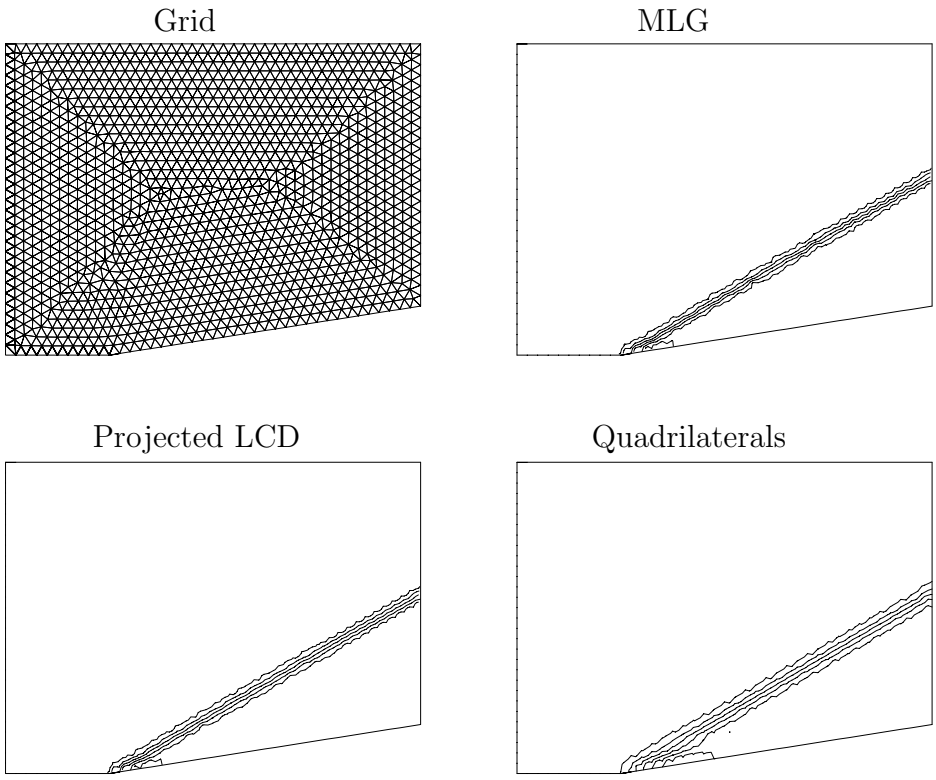

Figure 3.1: Grid and depth contours for the oblique hydraulic jump test case.

velocity everywhere. The 3688 cell grid on which the calculations were carried out is shown in Figure 3.2. Each of the boundaries is treated as a solid wall except those on the left and right which were given simple non-reflecting boundary conditions.

Figure 3.2 also shows the surface elevation of the water at $t = 7.2$s for the MLG and projected LCD schemes (using the grid shown) and a superbee limited scheme on a uniform 50×50 quadrilateral grid. The projected LCD scheme seems to give a slightly smoother solution than the MLG scheme, and both appear to be better than the quadrilateral scheme in the sharpness of capturing of the downstream hydraulic jump. The dimensionally split scheme also appears to be tending towards instability within the downstream vortex created at the lower edge of the break. The result obtained using the projected LCD scheme is also pictured in Figure 3.3.

Finally, the schemes have been compared using a circular dam break test case.

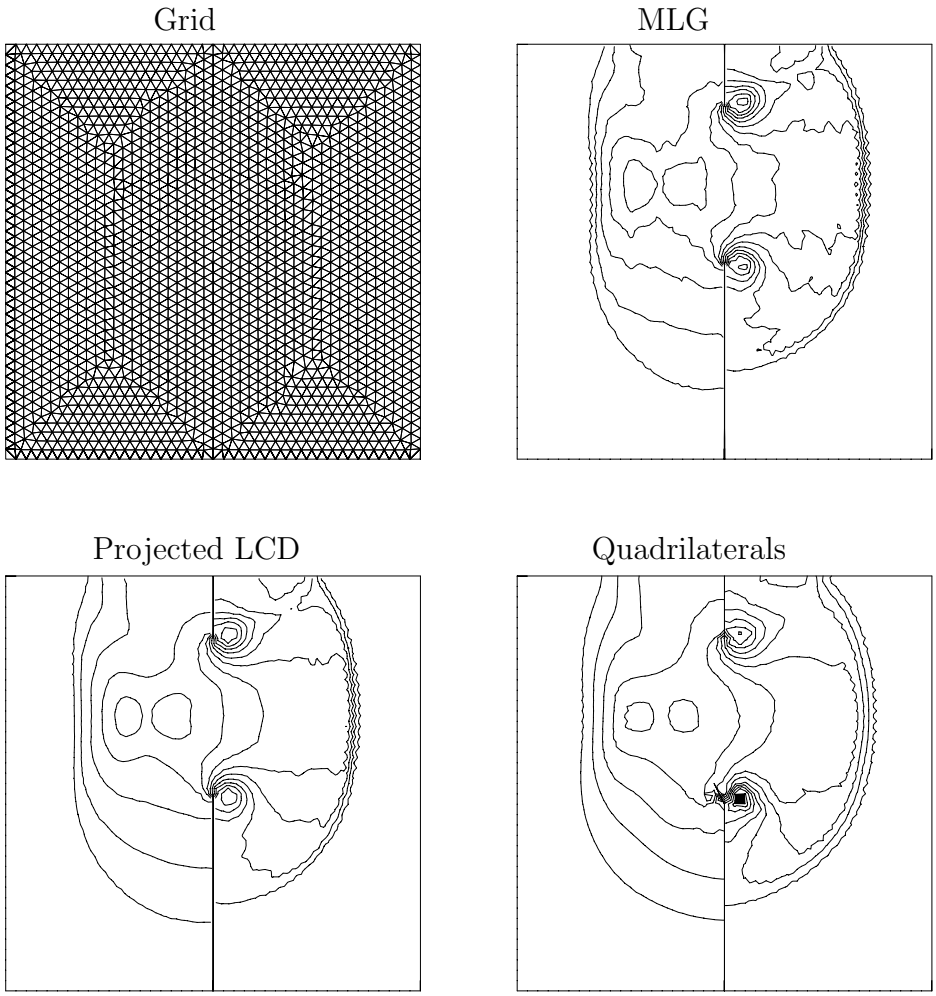

Figure 3.2: Grid and depth contours for the partial dam break test case.

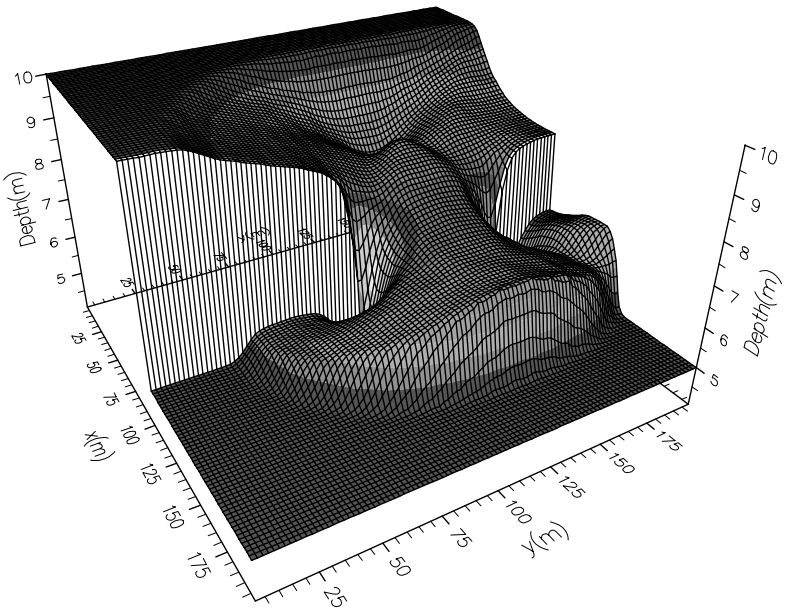

Figure 3.3: Projected LCD solution for the partial dam break test case.

Initially, two regions of still water are separated by a cylindrical wall (radius 11m) centred in the 50m $\times$ 50m square domain shown in Figure 3.4. The depth of the water is 10m within the cylinder and 1m outside. The wall is then removed and the solutions shown in Figures 3.4 and 3.5 are after $t = 0.69$s.

Once more, the solutions are very similar. The radial symmetry is slightly distorted by the effects of the grid in each case, but otherwise the solutions are very accurate. In all cases the MLG and projected LCD schemes have given similar solutions but the extra speed of the new scheme gives it the advantage in terms of efficiency.

4 Conclusions

In this paper the construction, on triangular grids, of second order accurate, cell centre finite volume schemes which satisfy a local maximum principle has been discussed.

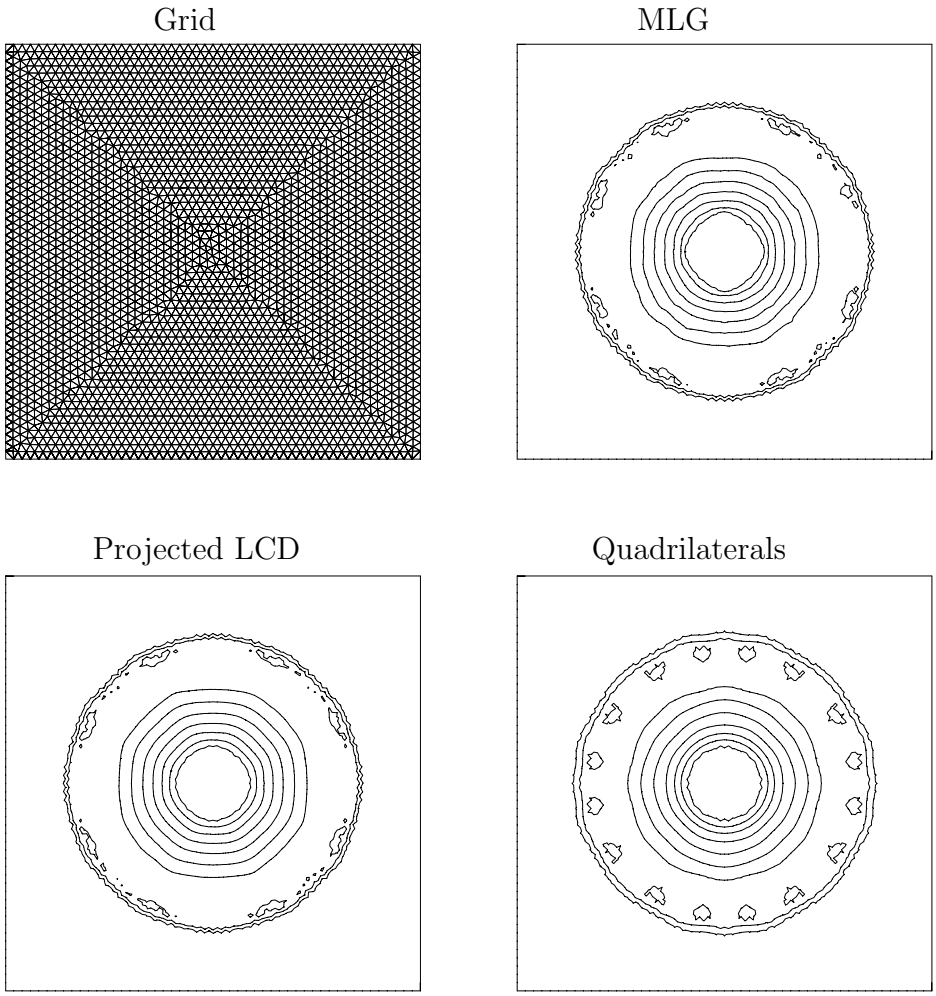

Figure 3.4: Grid and depth contours for the circular dam break test case.

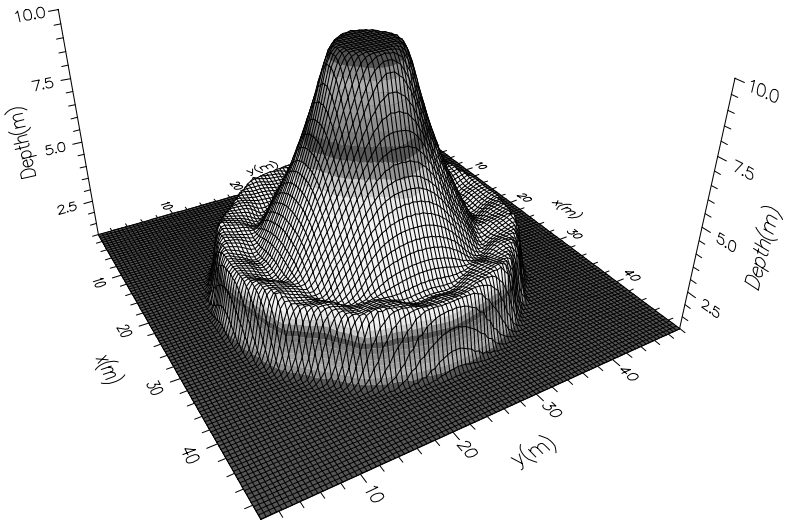

Figure 3.5: Projected LCD solution for the circular dam break test case.

The methods are based on MUSCL-type schemes [18] in two dimensions in which a linear reconstruction of the solution is created within each cell from local data, the gradient of which is limited to impose the desired local maximum principle on the approximation. The methods have been tested on the scalar advection equation and then extended to nonlinear systems of equations via Roe's approximate Riemann solver.

The limiters which satisfy the maximum principle are defined using constraints applied at the midpoints of the edges of the cells. It has been shown that these constraints define a region within which every limiter of the chosen type lies. Having defined this region, it is possible to use the multidimensional nature of the problem to apply a new limiting strategy to the existing schemes which improves their accuracy. It is also possible to construct new schemes using these ideas, but this has been left as a subject for future research. The 'projected' limiter schemes are cheaper than the

most accurate of the previously constructed limiters, and in the scalar case it is often considerably more accurate.

The scalar schemes have also been successfully applied to the shallow water equations using Roe's scheme, and accurate results have been obtained by applying the limiting procedure to the conservative variables. Although the improvement in accuracy obtained by using the new scheme is less apparent than in the scalar case, it is still significantly more efficient than the best of the existing schemes. Research into more robust and accurate treatments of source terms and boundary conditions associated with the shallow water equations is ongoing.

Acknowledgements

The author would like to thank Prof. M. J. Baines for his contributions to this work and the EPSRC for providing the funding for the author.

References

[1] F.Alcrudo and P.Garcia-Navarro, 'A high resolution Godunov-type scheme in finite volumes for the 2d shallow water equations', *Int. J. for Num. Methods in Fluids*, **16**:489–505, 1993.

[2] P.Batten, C.Lambert and D.M.Causon, 'Positively conservative high-resolution convection schemes for unstructured elements', *Int. J. for Num. Methods in Eng.*, **39**:1821–1838, 1996.

[3] T.J.Barth and D.C.Jesperson, 'The design and application of upwind schemes on unstructured meshes', *AIAA Paper 89-0366*, 1989.

[4] L.J.Durlofsky, B.Engquist and S.Osher, 'Triangle based adaptive stencils for the solution of hyperbolic conservation laws', *J. Comput. Phys.*, **98**:64–73, 1992.

[5] R.J.Fennema and M.H.Chaudry, 'Explicit methods for 2-D transient free-surface flows', *J. Hydraul. Eng. ASCE*, **116**:1013–1034, 1990.

[6] J.B.Goodman and R.J.LeVeque, 'On the accuracy of stable schemes for 2D conservation laws', *Math. Comp.*, **45**:15–22, 1985.

[7] C.Hirsch, *Fundamentals of Numerical Discretization*, volume 1 of *Numerical Computation of Internal and External Flows*, Wiley, 1990.

[8] M.E.Hubbard, 'Multidimensional slope limiters for MUSCL-type finite volume schemes', Numerical Analysis report 2/98, Department of Mathematics, University of Reading, 1998.

[9] M.E.Hubbard and M.J.Baines, 'Conservative multidimensional upwinding for the steady two-dimensional shallow water equations', *J. Comput. Phys.*, **138**:419–448, 1997.

[10] A.Jameson, 'Positive schemes and shock modeling for compressible flows', *Int. J. for Num. Methods in Fluids*, **20**:743–776, 1995.

[11] R.J.LeVeque, *Numerical Methods for Conservation Laws*, Birkhäuser, 1992.

[12] X.-D.Liu, 'A maximum principle satisfying modification of triangle based adaptive stencils for the solution of scalar hyperbolic conservation laws', *SIAM J. Numer. Anal.*, **30**:701–716, 1993.

[13] B.Perthame and Y.Qiu, 'A variant of van Leer's method for multidimensional systems of conservation laws', *J. Comput. Phys.*, **112**:370–381, 1994.

[14] P.L.Roe, 'Approximate Riemann Solvers, parameter vectors, and difference schemes', *J. Comput. Phys.*, **43(2)**:357–372, 1981.

[15] S.P.Spekreijse, 'Multigrid solution of monotone second-order discretizations of hyperbolic conservation laws', *Math. Comp.*, **49**:135–155, 1987.

[16] P.K.Sweby, 'High resolution schemes using flux limiters for hyperbolic conservation laws', *SIAM J. Numer. Anal.*, **21**:995–1011, 1984.

[17] B.van Leer, 'Towards the ultimate conservative difference scheme V. A second order sequel to Godunov's method', *J. Comput. Phys.*, **32**:101–136, 1979.

[18] B.van Leer, 'On the relation between the upwind-differencing schemes of Godunov, Engquist-Osher and Roe', *SIAM J. Scientific Statist. Comput.*, **5**, 1984.

[19] P.R.Woodward and P.Collela, 'The numerical simulation of two-dimensional fluid flow with strong shocks', *J. Comput. Phys.*, **54**:115–173, 1984.

A The Shallow Water Equations

The shallow water equations depend on the conservative variables and fluxes given by

$$\underline{U} = \begin{pmatrix} h \\ hu \\ hv \end{pmatrix}, \quad \underline{F} = \begin{pmatrix} hu \\ hu^2 + \frac{gh^2}{2} \\ huv \end{pmatrix}, \quad \underline{G} = \begin{pmatrix} hv \\ huv \\ hv^2 + \frac{gh^2}{2} \end{pmatrix}, \tag{A.1}$$

where h is the depth of the flow, u and v are the x- and y-velocities and g is the acceleration due to gravity, and result in the following flux Jacobians:

$$\mathbf{A} \;=\; \frac{\partial \underline{F}}{\partial \underline{U}} \;=\; \begin{pmatrix} 0 & 1 & 0 \\ c^2-u^2 & 2u & 0 \\ -uv & v & u \end{pmatrix}, \quad \mathbf{B} \;=\; \frac{\partial \underline{G}}{\partial \underline{U}} \;=\; \begin{pmatrix} 0 & 0 & 1 \\ -uv & v & u \\ c^2-v^2 & 0 & 2v \end{pmatrix}, \tag{A.2}$$

where $c = \sqrt{gh}$ is the gravity wave speed.

In Roe's approximate Riemann solver the eigenvalues and eigenvectors of the matrix

$$(\mathbf{A},\, \mathbf{B}) \cdot \vec{n} \;=\; \begin{pmatrix} 0 & n_x & n_y \\ (c^2-u^2)n_x - uvn_y & 2un_x - vn_y & un_y \\ -uvn_x + (c^2-v^2)n_y & vn_x & un_x + 2vn_y \end{pmatrix} \tag{A.3}$$

are

$$\lambda_1 \;=\; \tilde{u}n_x + \tilde{v}n_y + \tilde{c}\,, \quad \lambda_2 \;=\; \tilde{u}n_x + \tilde{v}n_y\,, \quad \lambda_3 \;=\; \tilde{u}n_x + \tilde{v}n_y - \tilde{c}\,, \tag{A.4}$$

and

$$\underline{r}_1 \;=\; \begin{pmatrix} 1 \\ \tilde{u} + \tilde{c}n_x \\ \tilde{v} + \tilde{c}n_y \end{pmatrix}, \quad \underline{r}_2 \;=\; \begin{pmatrix} 0 \\ -\tilde{c}n_y \\ \tilde{c}n_x \end{pmatrix}, \quad \underline{r}_3 \;=\; \begin{pmatrix} 1 \\ \tilde{u} - \tilde{c}n_x \\ \tilde{v} - \tilde{c}n_y \end{pmatrix}, \tag{A.5}$$

respectively, and the corresponding wave strengths in (3.5) are given by

$$\begin{aligned} \tilde{\alpha}_1 &= \frac{\Delta h}{2} + \frac{1}{2\tilde{c}}\left(\Delta(hu)n_x + \Delta(hv)n_y - (\tilde{u}n_x + \tilde{v}n_y)\Delta h\right) \\ \tilde{\alpha}_2 &= \frac{1}{\tilde{c}}\left(\left(\Delta(hv) - \tilde{v}\Delta h\right)n_x - \left(\Delta(hu) - \tilde{u}\Delta h\right)n_y\right) \\ \tilde{\alpha}_3 &= \frac{\Delta h}{2} - \frac{1}{2\tilde{c}}\left(\Delta(hu)n_x + \Delta(hv)n_y - (\tilde{u}n_x + \tilde{v}n_y)\Delta h\right)\,, \end{aligned} \tag{A.6}$$

in which the Roe average states are

$$\tilde{u} \;=\; \frac{u_R\sqrt{h_R} + u_L\sqrt{h_L}}{\sqrt{h_R} + \sqrt{h_L}}\,, \quad \tilde{v} \;=\; \frac{v_R\sqrt{h_R} + v_L\sqrt{h_L}}{\sqrt{h_R} + \sqrt{h_L}}\,, \quad \tilde{c} \;=\; \sqrt{\frac{g(h_R + h_L)}{2}}\,, \tag{A.7}$$

and the difference operator is given by

$$\Delta\cdot \;=\; (\cdot)_R - (\cdot)_L \;. \tag{A.8}$$

In two dimensions the subscripts $\cdot_L$ and $\cdot_R$ represent the interior and exterior edge midpoint values relative to the cell under consideration.